Journal of Mines, Metals and Fuels, *73(4): 1135-1146; 2025. DOI: 10.18311/jmmf/2025/47612*

Print ISSN : 0022-2755

Journal of Mines, Metals and Fuels

Contents available at: *www.informaticsjournals.co.in/index.php/jmmf*

Impact of Sintering Temperature on the Structural, Optical, and Dielectric Properties of Er_2O_3-doped ZrO_2 Ceramics Synthesized via Solid-State Reaction

M. Naga Sravanthi* and J. Sudagar

Department of Physics, School of Advanced Sciences (SAS), VIT-AP University, Near Vijayawada - 522241, Andhra Pradesh, India; nagasravanthi.20phd7125@vitap.ac.in

Abstract

Er_2O_3-doped zirconium dioxide ceramic samples were successfully synthesized using the solid-state reaction method at various sintering temperatures. The synthesized samples were analyzed using XRD, FESEM, EDAX, FTIR, and UV-Vis spectroscopy, and their dielectric properties-including dielectric constant (ε'), dielectric loss (ε''), and AC conductivity (σ_{ac})-were measured at ambient temperature. The average particle sizes calculated from the XRD spectra indicated an increase in particle size as the sintering temperature rose. The optical properties analyzed using a UV-Vis spectrophotometer revealed a reduction in band gap energy with increasing sintering temperature, which can be attributed to the growth in particle size. EDS analysis showed no impurities or unexpected elements, confirming the purity and controlled doping of Er_2O_3 in the ZrO_2 samples. The dielectric constant and dielectric loss of Er_2O_3-doped ZrO_2 exhibited a noticeable decrease with increasing frequency (Maxwell-Wagner polarization). Additionally, both ε' and ε'' were greater in the lower frequency range.

***Major Findings:** The study reveals that increasing the sintering temperature enhances crystallite size and improves the structural and optical properties of Er_2O_3-doped ZrO_2 ceramics. The dielectric constant and dielectric loss exhibit frequency-dependent behaviour, with higher values at lower frequencies, attributed to space charge polarization. The reduction in band gap with increasing sintering temperature suggests improved crystallinity and grain growth.*

Keywords: Dielectrical, Er_2O_3, Optical, Rare-earth Oxide, ZrO_2.

1.0 Introduction

Dielectric oxides have been integral to microelectronics, optics, and sensors for many years, owing to their distinctive features, including strong thermal stability, high dielectric constant, substantial refractive index, wide band gap, and high ionic conductivity[1,2]. In recent years, researchers have focused on developing materials for silicon-based dielectric devices to enhance storage density in dynamic random access memory, fabricate very large scale integrated circuits, develop gate dielectrics, prevent chemical corrosion, mitigate oxidation in metals, and detect oxygen. Consequently, Zirconium Oxide (ZrO_2) is a viable candidate due to its high dielectric constant, low toxicity, elevated band gap, and eco-friendliness compared to other ceramic oxides[3-8]. The characteristics of ZrO_2-based devices are significantly influenced by their phase structure and crystallite size. It is generally known that 100% ZrO_2 exhibits three polymorphs: Cubic, tetragonal, and monoclinic. The stable form at room temperature is the monoclinic phase, which transforms to the tetragonal phase around 1170° C during heating,

**Author for correspondence*

and subsequently to the cubic phase at 2370° C[9,10]. Due to its unique physical and chemical properties, the limited existing literature on the creation and characterization of these materials positions them as promising candidates for new advancements. A notable characteristic of ZrO_2 is its n-type semiconducting nature, featuring a wide band gap of approximately 5-6 eV, as highlighted by various researchers, including K. Anandan *et al.*[11]. Among its phases, the monoclinic structure is the most stable and suitable for diverse applications, such as gas sensors utilizing Cu-ZrO_2 nanomaterials[12]. Other applications include the catalytic properties of hydroxyl groups on Cu-ZrO_2 nanoparticles, the development of MOS-based capacitors incorporating Mg ions into ZrO_2, yttria-stabilized zirconia for fuel cells, and silicon-based zirconia MOS capacitors[13-16]. High-k gate dielectrics, including HfO_2, Y_2O_3, Al_2O_3, TiO_2, CuO, ZnO, and ZrO_2, have gained significant traction in oxide Thin Film Transistors (TFTs) due to their elevated dielectric constants and effective interface formation with oxide semiconductors, among these high-k materials, zirconium oxide is particularly noteworthy for its extensive applications in microelectronics and nanoelectronics, establishing it as one of the most promising alternative materials[17,18]. To prevent the transformation of ZrO_2 from cubic or tetragonal phases to the monoclinic phase, these dielectric materials have been blended with metal oxides, including lanthanides like lanthanum, as well as gadolinium, erbium, and dysprosium[19,20]. Additionally, cubic or tetragonal ZrO_2 layers with thicknesses ranging from 5 to 20 nm can be stabilized by interleaving them with films of varying chemical compositions, creating nanolaminate structures[21].

In this research, zirconium dioxide was combined with Erbium Oxide (Er_2O_3). Erbium oxide features a very narrow absorption band, which imparts a pink hue to erbium salts[22]. It has been extensively researched as a material for optical waveguides and as a dopant in optical amplifiers[23]. Some studies have focused on the growth and evaluation of Er_2O_3 films as potential high-k gate oxide materials[24]. Like other rare earth elements, erbium can modify the charge state of oxygen vacancies and help passivate gap states caused by these vacancies[25]. Combining Er_2O_3 with other high-k materials can enhance permittivity while maintaining the band gap and minimizing leakage currents[20]. NumEr_2O_3us studies have provided both experimental and theoretical evidence of higher k-values for different crystalline forms of ZrO_2, where elements such as Al, Y, Ge, and La are incorporated through doping or during the deposition of thin films. Moreover, the crystalline phase of the resulting product can be influenced by the type and concentration of the dopant, as well as the method of synthesis employed. Furthermore, we present the performance of erbium-doped ZrO_2 achieved through solid-state sintering at various temperatures for the first time. The incorporation of erbium ions into the host lattice is expected to enhance its structural, optical, magnetic, and dielectric properties, making it suitable for the production of microwave devices. The choice of erbium as a dopant in the ZrO_2 matrix is based on several key properties: (a) Erbium acts as a strong oxidizing agent. (b) Its electronic configuration of [Xe] $4f^{12}6s^2$ makes it particularly suitable for energy storage applications, such as super capacitors, enhancing cyclic stability due to its 17 multiple transition levels (including $4I_{15}/_2$, $4I_{13}/_2$, $4I_{11}/_2$, and others), which exhibit significant spin-orbit coupling. (c) Incorporating erbium into the zirconia [Kr] ($4d^2$ outer shell) matrix contributes to higher specific capacitance, allowing for greater charge storage per unit mass and an increased surface area. (d) The presence of erbium ions also facilitates faradaic redox reactions and enables efficient exchange of electrons and ions in the electrolyte during cyclic processes.

Various synthesis methods have been proposed for fabricating different types of oxide ceramics, including solid-state reactions, co-precipitation, sol-gel processes, slip casting, and microwave irradiation techniques. The solid-state reaction method has garnered significant interest due to several advantages: It is simple, requiring no intricate equipment; cost-effective, relying on affordable raw materials and tools; and easily scalable for large-scale production. This study focuses on the development of leading materials with improved structural, dielectric, and optical properties for a range of high-performance applications. In particular, we examine oxide ceramics combined with the rare earth element Er_2O_3. These oxide materials were carefully synthesized using the solid-state reaction method, followed by in-depth analysis to explore their properties and potential uses.

2.0 Experimental Details

2.1 Sample Preparation Method

Zirconium dioxide (ZrO_2, 5 µm, 99% purity, sourced from Sigma-Aldrich) and Erbium Oxide (Er_2O_3, 98% purity, obtained from SRL) were used as the main components. A ceramic oxide composed of 0.15 mol% erbium oxide doped with 0.85 mol% ZrO_2 was fabricated using the solid-state reaction method at various temperatures. These oxides were carefully blended in exact proportions using an agate mortar and pestle to prevent contamination from magnetic impurities. The resulting mixture was then heated in a tubular furnace chamber at 1000° C for 10 hours, with a heating rate of 5° C per minute. After cooling, a 5% Polyvinyl Alcohol (PVA) binder was incorporated, and the mixture was re-grinded for two hours. A portion of the sample was compressed under a pressure of 250 MPa to create pellets measuring 5 mm in radius and 2 mm in thickness. These pellets were then sintered at 1100° C, 1200° C, and 1300° C for eight hours in an alumina crucible inside the tubular furnace, with a heating rate of 5° C per minute. After cooling to Room Temperature (RT), the samples were labelled as ZE-11, ZE-12, and ZE-13. Sample codes are given in Table 1. A flow chart of the sample preparation method is shown in Figure 1.

Table 1. Sample codes

Si.No	Sample Code	Sintering Temperature
1	ZrO_2	Room temp
2	ZE-11	1100° C
3	ZE-12	1200° C
4	ZE-13	1300° C

2.2 Characterization Technique

The XRD pattern of ZrO_2 nanoparticles doped with erbium oxide was recorded using a Rigaku MiniFlex X-ray diffractometer. CuKα radiation (λ = 1.54059 Å) was employed as the X-ray source. Data collection was performed over a diffraction angle range of 10° to 90° at a scanning speed of 5.0°/min with a step size of 0.01 degrees. The FTIR spectrum of the nanoparticles with cerium-doped zirconium dioxide was acquired using an Agilent Cary 630 FTIR spectrometer, spanning a range of 400 to 4000 cm^{-1}. The optical band gap was assessed by

Table 2. Purpose of the characterization methods

Si. No	Characterization Methods	Purpose of the Study
1	XRD	Crystalline structure, phase composition, and lattice parameters of a material.
2	FESEM	Surface morphology and microstructural features of a material with high resolution.
3	EDAX	Elemental composition analysis and mapping of a material.
4	FTIR	Functional groups and analyze the chemical bonding in a material.
5	UV-vis	Optical properties and electronic transitions of a material.
6	Impedance analyzer	Electrical properties of materials, including impedance, capacitance, and dielectric behavior over a range of frequencies.



Figure 1. Flow chart for sample fabrication technique.

capturing the UV-Vis Diffuse Reflectance Spectroscopy (DRS) spectra with a PerkinElmer LAMBDA 365 instrument across a wavelength range of 200 to 1 100 nm.

The surface morphology of the mixed oxides was examined using a Field Emission Scanning Electron Microscope (FESEM), specifically a ZEISS model. Elemental composition analysis was performed using Energy Dispersive X-ray Spectroscopy (EDS) with an EDAX-EDS-SDD system (EDAX Inc., USA). The dielectric properties of all samples were measured using an IM3533-01 LCR meter across a frequency range of 1 mHz to 200 kHz under ambient temperature conditions. Purpose of the characterization techniques are listed in Table 2.

3.0 Results and Discussions

3.1 X-ray Diffraction

Figure 2 presents the XRD analysis of pure ZrO_2 and the synthesized samples ZE-11, ZE-12, and ZE-13. The XRD pattern of pure ZrO_2 confirmed the presence of monoclinic ZrO_2, with diffraction peaks identified at 2θ angles of 24.5°, 28.6°, 31.8°, 34.5°, 35.7°, 38.8°, and 41.1°, corresponding to the Miller Indices (hkl) values of [11-1], [111], [002], [200], [120], and [102], respectively. These values align with JCPDS card number 004-7563, which has a space group of P121/c1. In the ZE-11, ZE-12, and ZE-13 samples, two additional peaks at 2θ = 20.6° and 29.3° were observed, corresponding to the cubic phase of Er_2O_3 with (211) and (222) reflections, respectively[26]. The ZE-11 sample showed only the monoclinic phase of ZrO_2, while ZE-12 and ZE-13 displayed both monoclinic and tetragonal phases, with peaks at approximately 30°, 34.5°, 50°, and 60° corresponding to the (101), (110), (200), and (211) planes, respectively[27]. Crystallite size was calculated using the Debye-Scherrer formula. The average crystallite size for ZrO_2, ZE-11, ZE-12 and ZE-13 was mentioned in Table 3. The crystallite size increases with higher sintering temperatures due to enhanced atomic diffusion, as elevated temperatures provide greater atomic mobility, facilitating grain growth by reducing grain boundary energy. Smaller crystallites merge to form larger ones, and the increased energy at higher temperatures helps overcome activation barriers for nucleation and growth.

Interplanar spacing (d) for the oxide ceramic samples ZrO_2, ZE-11, ZE-12, and ZE-13 was calculated using Bragg's equation ($2d\sin\theta = n\lambda$). The average interplanar spacings for ZrO_2, ZE-11, ZE-12, and ZE-13 were recorded in Table 4. The increase in interplanar spacing with higher sintering temperatures can be attributed to thermal

Table 3. Average crystallite size for prepared samples

Si. No	Sample	Average Crystallite Size(nm)
1	ZrO_2	24
2	ZE-11	37.6
3	ZE-12	40.2
4	ZE-13	42.3

Table 4. Inter planar spacing for prepared samples

Si. No	Sample	Average d-spacing(A°)
1	ZrO_2	1.96
2	ZE-11	2.07
3	ZE-12	2.17
4	ZE-13	2.27

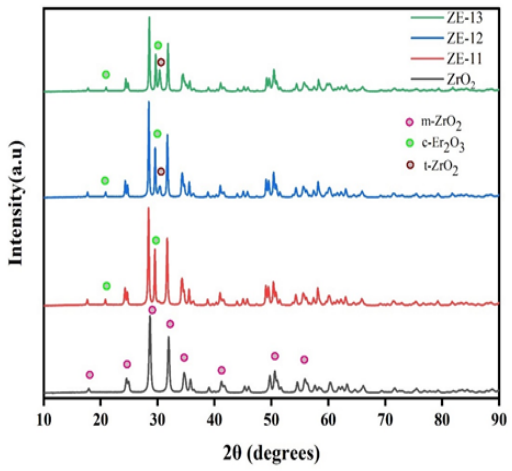


Figure 2. X-ray diffraction for ZrO_2, ZE-11, ZE-12 and ZE-13 samples.

expansion and structural changes within the material. As temperature rises, the lattice structure expands due to increased atomic vibrations, leading to greater distances between atomic planes. Additionally, higher sintering temperatures may promote phase transformations or changes in defect concentrations, contributing to the increased interplanar spacing.

3.2 Analysis of Morphology and Composition

Figure 3 illustrates the morphology and grain growth trends observed in the FESEM images of ZrO_2 and Er_2O_3-doped ZrO_2 samples sintered at different temperatures. Figure 3(a) shows the surface morphology of pure ZrO_2, highlighting the grain size, distribution, overall uniformity, and surface texture. Figure 3(b), representing the Er_2O_3-doped ZrO_2 sample sintered at 1100° C, reveals the early stages of grain formation. In Figure 3(c), which depicts the Er_2O_3-doped ZrO_2 sample sintered at 1200° C, more advanced grain growth is observed compared to Figure 3(b), with an apparent increase in grain size. Figure 3(d), corresponding to the Er_2O_3-doped ZrO_2 sample sintered at 1300° C, exhibits the most significant grain growth, characterized by larger grain sizes and reduced grain boundary areas. The increased temperature promotes greater atomic diffusion, leading to more pronounced grain growth. Additionally, doping ZrO_2 with Er_2O_3 influences grain growth and morphology compared to pure ZrO_2.

Analyzing the FESEM images of ZrO_2 and Er_2O_3-doped ZrO_2 samples sintered at different temperatures reveals several effects of Er_2O_3 doping:

Grain refinement- Compared to pure ZrO_2 (Figure 3a), the Er_2O_3-doped samples (Figure 3(b,c,d) show more defined grain boundaries and a more uniform, compact structure, particularly at 1200° C (Figure 3c).

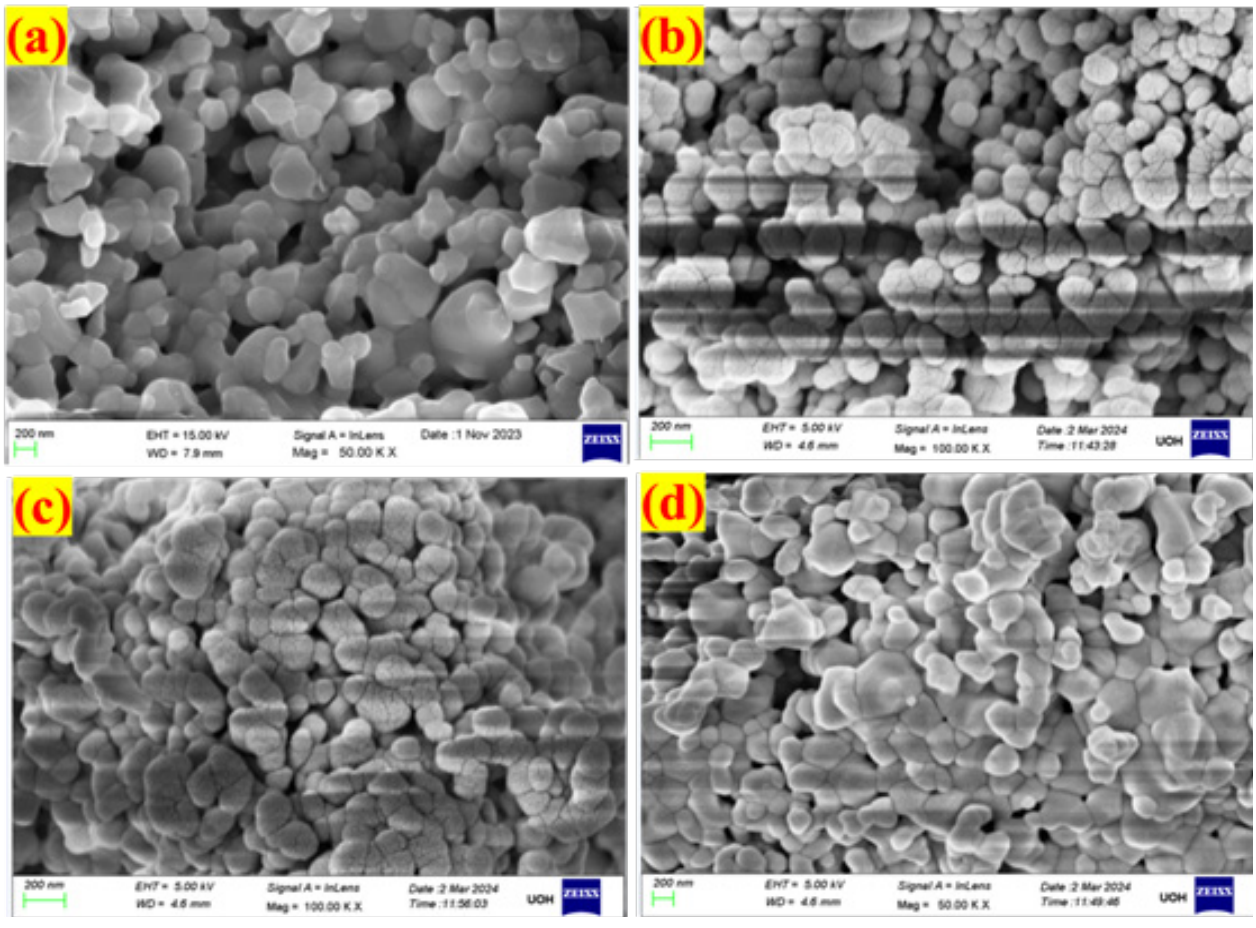


Figure 3. FESEM images of **(a)** ZrO_2, **(b)** ZE-11, **(c)** ZE-12 and **(d)** ZE-13 samples.

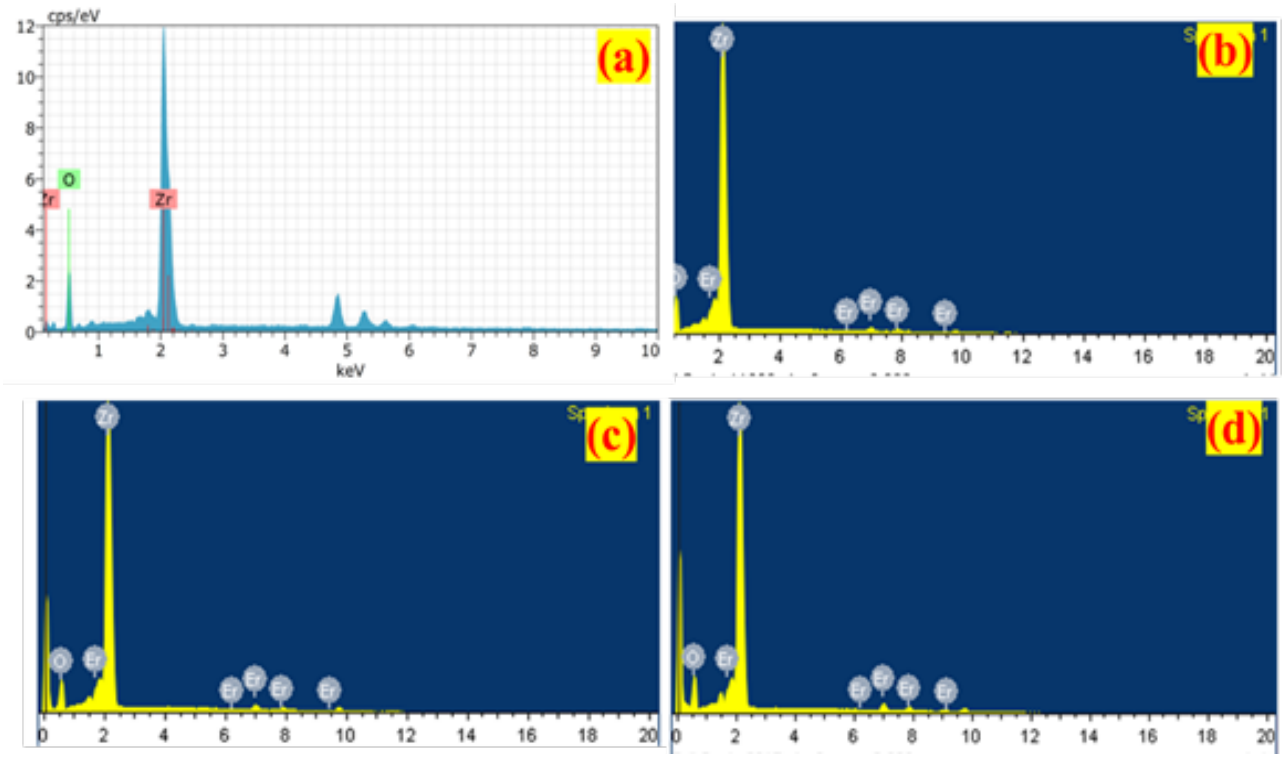


Figure 4. EDS analysis of **(a)** ZrO_2 **(b)** ZE-11 **(c)** ZE-12 **(d)** ZE-13 samples.

Grain growth with temperature- Grain size increases from 1100° C to 1300° C (Figures b-d), indicating that higher temperatures promote grain growth through enhanced atomic diffusion. While Er_2O_3 doping stabilizes the structure and influences growth kinetics, overall grain size continues to rise with temperature. Grain shape and density- As sintering temperature increases, grains become more pronounced and interconnected, especially at 1300° C (Figure 3d). Er_2O_3 doping enhances the densification of the ceramic, resulting in a more closely packed arrangement of grains at higher temperatures.

Homogeneity- The Er_2O_3-doped samples, particularly at 1200° C and 1300° C, display improved homogeneity in grain size distribution compared to undoped ZrO_2 (Figure 3a), suggesting that Er_2O_3 promotes a more consistent grain growth process.

Figure 4 presents the EDS analysis of ZrO_2 and the synthesized samples. Key observations from the EDX spectra of ZrO_2 and Er_2O_3-doped ZrO_2 sintered at different temperatures include:

ZrO_2 spectrum (Figure 4a)- The undoped ZrO_2 sample primarily shows peaks for Zirconium (Zr) and Oxygen (O), confirming the purity of the material with no additional elements present.

Er_2O_3-doped ZrO_2 at 1100° C (Figure 4b)- The EDX spectrum for the doped sample reveals peaks for Erbium (Er), alongside Zr and O. The lower intensity of the Er peaks is expected due to the doping concentration.

Er_2O_3-doped ZrO_2 at 1200° C (Figure 4c)- At this temperature, the Er peaks become more pronounced, indicating improved incorporation of erbium within the matrix, likely due to enhanced diffusion and interaction with the ZrO_2 structure.

Er_2O_3-doped ZrO_2 at 1300° C (Figure 4d)- The spectrum for the sample sintered at 1300° C shows the highest intensity of Er peaks, suggesting even better distribution of erbium. The Zr and O peaks remain prominent, and no unexpected elements are detected, confirming the composition's integrity.

3.3 Fourier Transform Infrared Spectroscopy (FTIR) Analysis

Figure 5 provides the FTIR spectra for ZrO_2 and synthesized samples. All spectra exhibit broad absorption bands, typically associated with the fundamental vibrational modes of metal-oxygen bonds, specifically Zr-O and possibly Er-O bonds due to doping. These

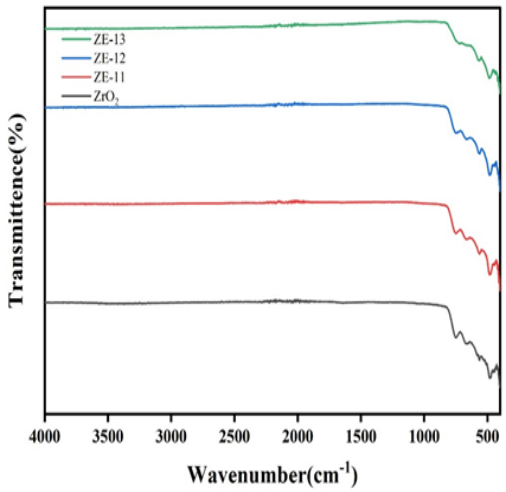


Figure 5. FTIR spectra for ZrO_2, ZE-11, ZE-12 and ZE-13 samples.

peaks are most prominent in the region around 500-800 cm^{-1}, indicating the characteristic vibrations of the ZrO_2 lattice[28]. The position and intensity of the absorption peaks slightly shift with increasing sintering temperature, indicating possible structural changes within the lattice. Higher sintering temperatures may influence the crystal structure and bonding characteristics, leading to these shifts. As sintering temperature increases (ZE-13 compared to ZE-11), the transmittance values increase across the wavenumber range, suggesting improved crystallinity and reduced lattice defects or impurities at higher temperatures. The doping of Er_2O_3 is likely causing subtle changes in the vibrational modes, though specific Er-related peaks may not be clearly distinguishable in this range. The overall spectra suggest the incorporation of Er_2O_3 into the ZrO_2 lattice and its effect on the structural properties of the material.

3.4 Ultraviolet-visible (UV-vis) Absorption Spectroscopy

Figure 6 shows optical band gap for ZrO_2 and synthesized samples. The light absorption properties of the synthesized samples in the UV-visible region were studied using diffuse reflectance spectra with range of wavelength 200-900 nm. The obtained reflectance data were converted into the Kubelka-Munk function, F(R), defined as: $F(R)=\frac{(1-R)^2}{2R}$. where R represents the sample's reflectance value. Additionally, the absorption edge values of the samples were determined by plotting the Kubelka-Munk function, F(R), against the band gap energy (E_g), as shown in Figure 6. The plots of $(F(R)\ \upsilon)^2$ against (υ) for the sintered samples at various temperatures are shown in Figure 6. Straight lines were fitted to the experimental curves and extended to intersect the (υ) axis, allowing the optical band gap values of ZrO_2 and Er_2O_3 doped with

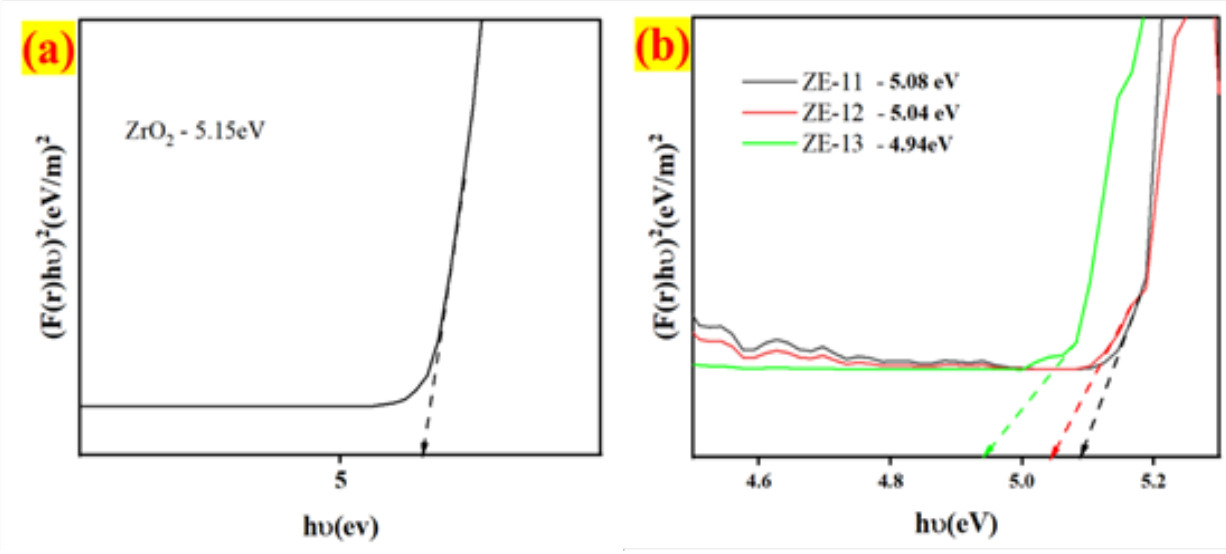


Figure 6. Energy band gap for **(a)** pure *ZrO_2*, **(b)** ZE-11, ZE-12 and ZE-13 samples.

ZrO_2 sintered at different temperatures to be determined. As shown in Figure 6, the band gap energy of ZrO_2 isapproximately 5.15 eV and for ZE-11,ZE-12 and ZE-13 are 5.08eV,5.04eV,and 4.94eV successively and catalogued in Table 5. The optical band gap was observed to reduce as the sintering temperature increased, dropping from 5.08 eV at 1100° C to 4.94 eV at 1300° C. This reduction in the energy band gap with higher sintering temperatures is attributed to particle growth and enhanced crystallinity, as confirmed by XRD analysis[29]. As sintering temperature increases, particle sizes tend to grow. Larger particle sizes lead to a reduction in quantum confinement effects, which can decrease the band gap. Higher sintering temperatures often lead to better crystallinity of the material. Improved crystallinity reduces defects and lattice strain, which also can lower the band gap.

Table 5. Band gap of fabricated samples

Si.No	Sample	Band Gap(eV)
1	ZrO_2	5.15
2	ZE-11	5.08
3	ZE-12	5.04
4	ZE-13	4.94

3.5 Analysis of Dielectrical Properties

The dielectric constant (ε') of both undoped and Er_2O_3-doped ZrO_2 ceramics was examined over a frequency range of 1 Hz to 200 kHz at room temperature using an impedance analyzer. The dielectric constant, also known as relative permittivity, reflects a materials ability to polarize in response to an applied electric field. This dimensionless value is defined as the ratio of a materials permittivity to that of free space. The dielectric constant measures the level of polarization in a dielectric material when exposed to an external electric field. As the polarization increases, so does the dielectric constant. Several factors, including the materials chemical composition and the production process, influence its dielectric properties.

The dielectric constant (ε') is an important metric for evaluating the dielectric properties of high-k materials. Figure 7 demonstrates the relationship between the dielectric constant and frequency for pure ZrO_2 and ZrO_2/Er_2O_3 mixed oxides at Room Temperature (RT). At lower frequencies, ε′ increases but decreases with rising frequency, which is due to a reduction in space charge polarization effects. The high ε′ values observed at low frequencies can be explained by the Maxwell-Wagner model, emphasizing the influence of grain boundaries on space charge polarization. This behaviour is consistent with the Debye relaxation model, particularly in relation to orientational polarization. In many dielectric materials, the dielectric constant tends to stabilize at higher frequencies, as the electric dipoles are unable to keep pace with the rapid fluctuations of the alternating applied electric field[30]. Koop's phenomenological theory suggests that at lower frequencies, the dielectric value is primarily influenced by the conductivity of the grain boundaries. This is due to the increased effectiveness of grain boundaries in conducting at these frequencies, resulting in a higher permittivity. As the frequency increases, however, the permittivity decreases.

The higher dielectric constant observed for the sample sintered at 1100° C (ZE-11) compared to those sintered at higher temperatures (ZE-12 and ZE-13). At lower sintering temperatures (such as 1100° C for ZE-11), the grain size may remain smaller, leading to more grain boundaries. These grain boundaries are known to contribute significantly to space charge polarization, which enhances the dielectric constant, especially at low frequencies. As the sintering temperature increases, grain growth occurs, reducing the number of grain boundaries and thus diminishing the space charge contribution to the dielectric constant. Sintering at higher temperatures (1200° C and 1300° C) often improves the crystallinity of the material, which can reduce defects, vacancies, and grain boundary areas. While improved crystallinity typically enhances some properties (like electrical conductivity), it reduces the contribution of grain boundary polarization, leading to a lower dielectric constant. The incorporation of Er_2O_3 might be more effective at lower temperatures, where the dopant ions can better interact with the ZrO_2 matrix, influencing the polarization behaviour. At higher temperatures, the dopant could become more homogeneously distributed, reducing its impact on localized polarization effects, which could lead to a decrease in the dielectric constant.

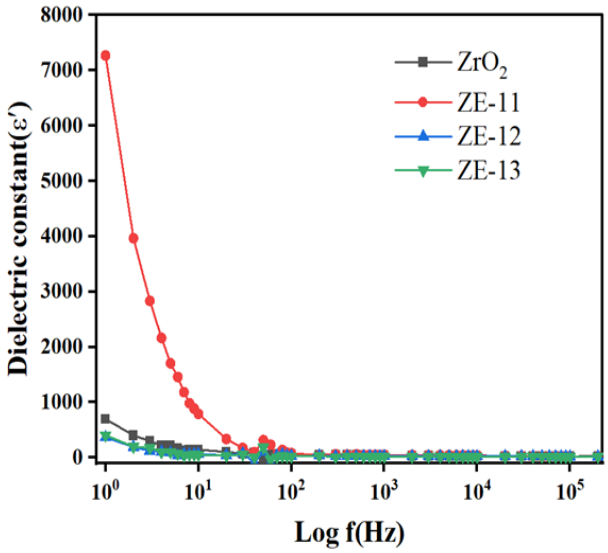


Figure 7. Frequency controlled dielectric constant (ε') for ZrO_2, ZE-11, ZE-12, and ZE-13 samples at RT.

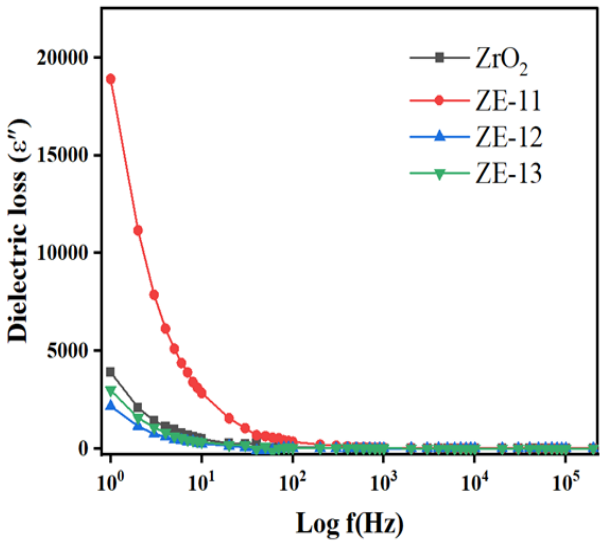


Figure 8. Frequency dependence dielectric loss (ε") for ZrO_2, ZE-11, ZE-12, and ZE-13 at RT.

Figure 7, the dielectric constant of pure ZrO_2 is relatively low compared to the doped samples and remains stable across the frequency range 1Hz to 200KHz. The sample doped with Er_2O_3 and sintered at 1100° C shows a significantly higher dielectric constant, especially at lower frequencies, reaching a peak value around 7000. However, the dielectric constant decreases rapidly as the frequency increases, which may be due to space charge polarization effects and the contribution of grain boundaries, as explained by the Maxwell-Wagner model. The dielectric constants of samples sintered at 1200° C and 1300° C (ZE-12 and ZE-13) are lower than that of the ZE-11 sample. These values decrease further as sintering temperature increases, likely due to changes in the microstructure and grain size at higher temperatures. The lower sintering temperature (1100° C) may not allow full densification of the material, leaving voids and defects, which increase energy dissipation and dielectric loss. Higher sintering temperatures (1200° C and 1300° C) lead to better densification and fewer defects, reducing dielectric loss.

Figure 8 shows the dielectric loss verses frequency of undoped and Er_2O_3 doped ZrO_2 at ambient temperature. Dielectric loss (ε") measured the following equation: $\varepsilon'' = \varepsilon' \times \mathrm{Tan}\,\delta$. The dielectric loss (ε") for the Er_2O_3-doped ZrO_2 sintered at 1100° C (ZE-11) is significantly higher compared to the samples sintered at 1200° C (ZE-12) and 1300° C (ZE-13). There is a sharp decline in dielectric loss as the frequency increases for all samples, but ZE-11 shows much higher values at lower frequencies compared to the other samples. The dielectric loss for ZE-12 and ZE-13 is relatively low and nearly similar across the frequency range, indicating improved stability at higher sintering temperatures.

Figure 9 presents the experimental results demonstrating the variation in AC conductivity ($\sigma_{ac} = \omega\varepsilon_0 \varepsilon' \tan\delta$) as a function of frequency, measured at room temperature across a frequency range of 1Hz to 200 kHz. From the Graph 9, it can be observed that the $\boldsymbol{\sigma}_{ac}$ elevates with frequency for all samples, and the conductivity is significantly higher for the sample sintered at 1100° C (ZE-11), followed by the samples sintered at 1200° C (ZE-12) and 1300° C (ZE-13), respectively. ZE-11 exhibits the highest AC conductivity, especially at higher frequencies. As the sintering temperature increases, the AC conductivity decreases, with ZE-13 showing the lowest conductivity. The increased AC conductivity for ZE-11 can be attributed to its microstructure, which might promote higher mobility of charge carriers. At lower sintering temperatures, grain boundaries are more prominent, contributing to increased space charge

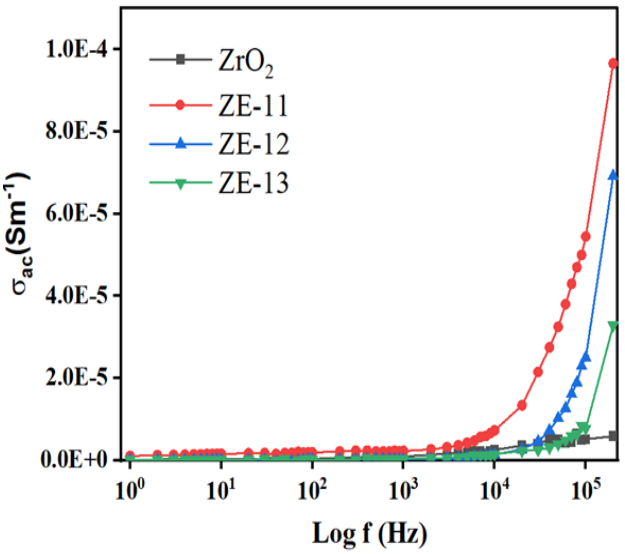


Figure 9. AC conductivity versus frequency for ZrO_2, ZE-11, ZE-12, and ZE-13 at RT.

polarization, which enhances conductivity. However, as the sintering temperature increases (ZE-12 and ZE-13), grain growth leads to a reduction in grain boundary density, thereby decreasing the contribution to AC conductivity.

4.0 Conclusion

Er_2O_3-doped ZrO_2 ceramics were synthesized via the solid-state reaction method and sintered at various temperatures, leading to the following observations:

1. **XRD Analysis:** The ZE-11 sample exhibited a monoclinic structure, while ZE-12 and ZE-13 showed a mixture of monoclinic and tetragonal phases. Higher sintering temperatures resulted in larger grain sizes.
2. **FESEM Findings:** Er_2O_3 doping promoted a uniform grain structure, enhanced grain boundary definition, and controlled grain growth. Increased densification at higher temperatures indicates that Er_2O_3 stabilizes the microstructure during sintering. EDAX analysis confirmed that the intensity of Er peaks increased with temperature, suggesting better incorporation of Er_2O_3 into the ZrO_2 lattice.
3. **FTIR Spectra:** Higher sintering temperatures led to increased crystallinity and structural changes in the ZrO_2-Er_2O_3 system, reflected by shifts in vibrational bands and increased transmittance.
4. **UV-vis Spectra:** The observed reduction in the band gap with rising sintering temperatures is attributed to increased particle size, improved crystallinity, and structural changes.
5. **Dielectric Properties:** The dielectric constant was highest for the ZE-11 sample sintered at 1100° C, decreasing with higher temperatures (ZE-12 and ZE-13). This decline is linked to reduced grain boundary polarization and microstructural features. Although ZE-11 exhibited higher dielectric loss due to increased grain boundary effects, the materials may be suitable for dielectric resonators, benefiting telecommunications and satellite applications due to their high-temperature stability and predictable dielectric behaviour.

5.0 Acknowledgement

The authors thank the VIT-AP and the VIT groups for their support in publishing this article. This work was supported by the RGEMS project (RGEMS2021016).

6.0 Authorship Contribution Statement

Sravanthi, M.N: Writing, original draft, methodology, formal analysis, conceptualization, resources, data curation. J. Sudagar: Visualization, validation, supervision, project administration, formal analysis.

7.0 References

1. Wilk GD, Wallace RM, Anthony J. High-κ gate dielectrics: Current status and materials properties considerations. J Appl Phys. 2001; 89(10):5243-5275. https://doi.org/10.1063/1.1361065
2. Rignanese GM, Gonze X, Jun G, Cho K, Pasquarello A. First-principles investigation of high-κ dielectrics: Comparison between the silicates and oxides of hafnium and zirconium. Phys Rev B. 2004; 69(18):184301. https://doi.org/10.1103/physrevb.69.184301
3. Sravanthi MN, Sudagar J. Structural, optical, and dielectric properties of zirconium titanate ceramic composite synthesized by solid-state reaction. J Mater

Eng Perform. 2023; 33:12133-12143. https://doi.org/10.1007/s11665-023-08827-z
4. Ibanez RL, Barrado JR, Martin F, Brucker F, Leinen D. Oxide barrier coatings on steel strip by spray pyrolysis. Surf Coat Technol. 2004; 188-189:675-683. https://doi.org/10.1016/j.surfcoat.2004.07.002
5. Sravanthi N, Sudagar J. Synthesis and properties of zirconium-cerium composite *via* solid-state route. Sci Sinter; 2024. p.18. https://doi.org/10.2298/sos240416018n
6. Taguchi M, Nakane T, Matsushita A, Sakka Y, Uchikoshi T, Funazukuri T, Naka T. One-pot synthesis of monoclinic ZrO_2 nanocrystals under subcritical hydrothermal conditions. J Supercrit Fluids. 2014; 85:57-61. https://doi.org/10.1016/j.supflu.2013.11.001
7. Sravanthi MN, Jothi S, Kumar AS. Effect of CeO_2 doped zirconium titanate with various temperatures by solid-state reaction method. Mater Sci Forum. 2023; 1107:93-104. https://doi.org/10.4028/p-7oyoml
8. Zhao C, Zhao CZ, Werner M, Taylor S, Chalker P. Dielectric relaxation of high-k oxides. Nanoscale Res Lett. 2013; 8:456. https://doi.org/10.1186/1556-276x-8-456
9. Barnard AS, Yeredla RR, Xu H. Modelling the effect of particle shape on the phase stability of ZrO_2 nanoparticles. Nanotechnol. 2006; 17(12):3039. https://doi.org/10.1088/0957-4484/17/12/038
10. Kumari L, Li W, Wang D. Monoclinic zirconium oxide nanostructures synthesized by a hydrothermal route. Nanotechnol. 2008; 19(19):195602. https://doi.org/10.1088/0957-4484/19/19/195602
11. Lovchinov K, Slavov L, Alexieva G, Ivanov P, Marinov G, Gergova R, Strijkova V, Babeva T. Study of ZrO_2 nanolayers deposited electrochemically on different conductive substrates. Mater Sci Semicond Process. 2021; 131:105843. https://doi.org/10.1016/j.mssp.2021.105843
12. Hemalatha E, Gopalakrishnan N. Gas sensing performances of pure and Cu-doped ZrO_2 nanostructures. Appl Phys A. 2019; 125(493). https://doi.org/10.1007/s00339-019-2789-0
13. Reddy CV, Reddy IN, Ravindranadh K, Reddy KR, Shetti NP, Kim D, Shim J, Aminabhavi TM. Copper-doped ZrO_2 nanoparticles as high-performance catalysts for efficient removal of toxic organic pollutants and stable solar water oxidation. J Environ Manag. 2020; 260:110088. https://doi.org/10.1016/j.jenvman.2020.110088
14. Bhanu JU, Babu GR, Thangadurai P. Influence of Mg ion concentration in ZrO_2 gate dielectric layered silicon-based MOS capacitors for memory applications: Thorough understanding of conduction processes. Mater Sci Semicond Process. 2019; 89:85-96. https://doi.org/10.1016/j.mssp.2018.09.004
15. Sigwadi R, Mokrani T, Dhlamini M. The synthesis, characterization, and electrochemical study of zirconia oxide nanoparticles for fuel cell application. Phys B Condens Matter. 2020; 581:411842. https://doi.org/10.1016/j.physb.2019.411842
16. Bhanu JU, Amutha A, Babu GR, Sundaravel B, Thangadurai P. Crystalline phase dependent electrical properties of Mg incorporated tetragonal phase stabilized ZrO_2 high-κ dielectric layer in Si based MOS capacitors. Mater Sci Semicond Process. 2018; 81:7-16. https://doi.org/10.1016/j.mssp.2018.02.031
17. Gao Y, Li X, Chen L, Shi J, Sun XW, Zhang J. High mobility solution-processed hafnium indium zinc oxide TFT with an Al-doped ZrO_2 gate dielectric. IEEE Elect Device L. 2014; 35(5):554-556. https://doi.org/10.1109/led.2014.2310120
18. Dutta S, Pandey A, Yadav I, Thakur OP, Kumar A, Pal R, Chatterjee R. Growth and electrical properties of spin-coated ultrathin ZrO_2 films on silicon. J Appl Phys. 2013; 114:014105. https://doi.org/10.1063/1.4812733
19. Yamamoto Y, Kita K, Kyuno K, Toriumi A. Structural and electrical properties of HfLaOx films for an amorphous high-k gate insulator. Appl Phys Lett. 2006; 89(3):032903. https://doi.org/10.1063/1.2227630
20. Govindarajan S, Boscke TS, Sivasubramani P, Kirsch PD, Lee BH, Tseng HH, Jammy R, Schröder U, Ramanathan S, Gnade BE. Higher permittivity rare-earth doped HfO_2 for sub-45-nm metal-insulator-semiconductor devices. Appl Phys Lett. 2007; 91(6). https://doi.org/10.1063/1.2768002
21. Kukli K, Ihanus J, Ritala M, Leskela M. Properties of Ta_2O_5-based dielectric nanolaminates deposited by atomic layer epitaxy. J Electrochem Soc. 1997; 144:300. https://doi.org/10.1149/1.1837399
22. James C. A new method for the separation of the yttrium earths. J Am Chem Soc. 1907; 29(4):495-499. https://doi.org/10.1021/ja01958a010
23. Iacona F, Franzo G, Miritello M, Savio RL, Pecora EF, Irrera A, Priolo F. Er-based materials for Si microphotonics. Opt Mater. 2009; 31(9):1269-1274. https://doi.org/10.1016/j.optmat.2008.10.002
24. Jinesh KB, Lamy Y, Tois E, Besling WFA. Charge conduction mechanisms of atomic-layer-deposited Er_2O_3 thin films. Appl Phys Lett. 2009; 94(25). https://doi.org/10.1063/1.3159833

25. Tamm A, Heikkila M, Kemell M, Kozlova J, Kukli K, Sammelselg V, Ritala M, Leskela M. Atomic layer deposition and characterization of zirconium oxide-erbium oxide nanolaminates. Thin Solid Films. 2010; 519(2):666-73. https://doi.org/10.1016/j.tsf.2010.08.111
26. Bahi RE, Mahdi H, Mohamed D. Synthesis, characterization, optical, and electrical properties of polyvinyl alcohol or nano erbium oxide hybrid nanocomposites. J Inorg Organomet Polym Mater. 2024; 34:6114-6127. https://doi.org/10.1007/s10904-024-03244-8
27. Lee SW, Condrate RA. The infrared and Raman spectra of ZrO_2-SiO_2 glasses prepared by a sol-gel process. J Mater Sci. 1988; 23:2951-9. https://doi.org/10.1007/bf00547474
28. Yu Y, Wang X, Cao Y, Hu X. Study on the structure and properties of ZrO_2 buffer layers on stainless steel by XRD, IR and AES. Appl Surf Sci. 2001; 172(3-4):260-264. https://doi.org/10.1016/s0169-4332(00)00863-1
29. Keiteb AS, Saion E, Zakaria A, Soltani N. Structural and optical properties of zirconia nanoparticles by thermal treatment synthesis. J Nanomater. 2016. https://doi.org/10.1155/2016/1913609
30. Kambale RC, Shaikh PA, Bhosale CH, Rajpure KY, Kolekar YD. Dielectric properties and complex impedance spectroscopy studies of mixed Ni-Co ferrites. Smart Mater Struct. 2009; 18(8):085014. https://doi.org/10.1088/0964-1726/18/8/085014